nature astronomy

Article

https://doi.org/10.1038/s41550-024-02369-7

Evidence from 162173 Ryugu for the influence of freeze–thaw on the hydration of asteroids

Received: 8 August 2023

Accepted: 22 August 2024

Published online: 26 September 2024

Check for updates

Matthew J. Genge[1,2] ✉, Natasha V. Almeida[2], Matthias van Ginneken[3], Lewis Pinault[4], Penelope J. Wozniakiewicz[2,3] & Hajime Yano[5,6]

Hydrated asteroids are likely to be main source of water for the terrestrial planets. The controls on the extent of asteroid hydration, however, are poorly understood. Here we report the discovery of multiple fracture and vein sets in a sample from the C-type asteroid 162173 Ryugu that acted as pathways for the migration of distal fluids during its aqueous alteration. Early veins in Ryugu are decorated with framboidal magnetite, while later veins caused metasomatism of wall rocks. Both veins and fractures have cuspate geometries and complex intersecting geometries consistent with freeze–thaw fractures formed during experiments. We show that freeze–thaw is effective in fracturing C-type asteroids to up to 300 km in diameter and is thus crucial in the outwards migration of fluids in ice-bearing asteroids. Freeze–thaw is likely, therefore, to determine the distribution of mineral-hosted water in asteroids throughout the Cosmos.

The story of water in the Solar System is the story of habitable worlds. Ice condensed from nebula gas was incorporated into primitive asteroids during their accretion beyond the snow line[1] and melted during internal heating of these bodies in the early Solar System[2]. The melt water produced during this period caused hydration of primitive asteroids, transforming their primordial mineralogy into phyllosilicates, magnetite, sulfides and carbonates[3] and changing the diversity of organic molecules they contained[4]. It was these materials that were delivered to the early terrestrial planets to generate oceans and to seed organic materials that may have played a role in the origins of life[5].

Samples of carbonaceous asteroid 162173 Ryugu, returned by Japan Aerospace Exploration Agency's Hayabusa2 mission[6–9], have mineralogies, compositions and textures closely related to CI chondrites and, thus, have experienced substantial aqueous alteration in the early Solar System[10]. We report the discovery of unusual fractures and veins within sample A0180 from Ryugu that have not previously been observed within primitive meteorites. Comparison with experimental results indicates that these features formed by freeze–thaw of water ice in the Ryugu progenitor asteroid and that freeze–thaw is an important process in the migration and aqueous alteration of these objects.

Results

Nano computed tomography (nano-XCT) and scanning electron microscopy (SEM) of two serially polished mounts were used to characterize the three-dimensional (3D) morphologies and mineralogies of features within sample A0180. Fractures and veins comprise a small volume of the sample (0.24 vol% and 0.15 vol%, respectively) and are found within fine-grained, phyllosilicate-dominated matrix containing 1.42 vol% magnetite, 0.79 vol% sulfide, 1.4 vol% dolomite and no anhydrous silicate. Magnetite, sulfide and dolomite abundances are lower than other Ryugu samples[10].

Fractures in A0180 appear as curvilinear cracks up to 3 μm wide and have cuspate to sinusoidal geometries with characteristic wavelengths of 5–500 μm and tortuosity of 1.21–1.03 (mean 1.11; Fig. 1). Fractures appear as intersecting networks and as isolated cracks completely enclosed in matrix (Figs. 1b–d and 2). Short (<50 μm), thin fractures are observed cutting across larger curved fractures with intersection angles of ~90° (Fig. 1c–e,g). A small proportion (<10%) of large, curved fractures are subparallel to each other (Fig. 1a,b). Most fractures have tapering crack tips, which in overlapping, subparallel fractures are deflected towards each other (Fig. 1b). Where fractures

[1]Department of Earth Science and Engineering, Imperial College London, London, UK. [2]Planetary Materials Group, Natural History Museum, London, UK. [3]Centre for Astrophysics and Planetary Science, Department of Physics and Astronomy, University of Kent, Canterbury, UK. [4]Department of Earth and Planetary Sciences, Birkbeck College, London, UK. [5]Department of Interdisciplinary Space Science, Institute of Space and Astronautical Science, Japan Aerospace Exploration Agency, Sagamihara, Japan. [6]Space and Astronautical Science, Graduate Institute for Advanced Studies, Sagamihara, Japan. ✉e-mail: m.genge@imperial.ac.uk

encounter dolomite, magnetite or sulfide crystals, they circumnavigate one side of the crystal (Fig. 1a). Fractures are mostly occupied by void space and have matching opposing boundaries (Fig. 1d). Some fractures, however, are partially infilled with phyllosilicates (Fig. 1c,l). These healed cracks can be traced by their lower backscattered electron potentials (BEP) and usually extend to a crack termination. In addition, one crack is partly occupied by a Ni-bearing sulfide grain.

Halos of altered fine-grained matrix surround fractures and have a lower BEP than the rest of the matrix (Fig. 1b,l). The alteration halos extend 5–10 µm from the central fracture. The halo decreases in width towards crack terminations and is widest at fracture intersections. Similar low BEP halos also occur on the external surfaces of sample A0180 and are up to 50 µm wide—suggesting the sample was bounded by fractures (Fig. 1a). The matrix within halos is compositionally distinct from the surrounding material since it is depleted in Na and is more homogeneous, lacking Mg- and Si-rich areas, which are likely to be altered anhydrous silicates, pseudomorphed by phyllosilicate (Fig. 1i–k). The halos, therefore, appear to have experienced leaching by more intense aqueous alteration.

Sample A0180 also exhibits curvilinear bodies containing framboidal magnetite with interstitial phyllosilicate or void space and are discontinuous vein-like structures (Figs. 1e,f and 2), which can extend the full length of the particle (1 mm; Fig. 1f–k). These magnetite veins, like fractures, have cuspate to sinusoidal morphologies with characteristic wavelengths <500 µm and tortuosity (ratio of path to line length) of 1.28–1.02 (mean 1.11), similar to fractures. Some magnetite veins intersect to produce triple junctions, while others cross-cut, often with a thinner linear vein perpendicular to the wider cuspate vein (Fig. 1g,i). Subparallel magnetite veins are also observed. Tapering vein terminations occur in places, although the discontinuous nature of veins makes terminations uncertain. Where fractures and magnetite veins intersect, fractures cut across veins, suggesting they formed later (Fig. 1a). In the polished sections, several magnetite veins were seen to wrap around pre-existing mineral grains. Veins filled with framboidal magnetite have not been previously reported from CI chondrite meteorites.

Discussion

The formation mechanism of the fractures and veins within particle A0180 can be determined from their characteristic morphologies. Fractures within extraterrestrial samples are often assumed to form as a result of thermal expansion or weathering after arrival on Earth. The presence of infillings of phyllosilicate and sulfide, and alteration halos in A0180, however, indicate these are features originated on Ryugu and were once filled by aqueous fluids. An origin by interaction with terrestrial atmospheric water vapour can be discounted since the specimen was kept in a nitrogen atmosphere until immediately before nano-XCT analysis and no similar alteration occurred on the polished section once exposed to atmosphere.

The similar morphological features of fractures and veins suggest they formed by the same mechanism. The matching boundaries of fractures further indicate they opened under extension, which, owing to the presence of phyllosilicates and sulfides within them, must have been during aqueous alteration in the early Solar System. Several mechanisms exist for extensional fracturing on asteroids including thermal expansion, shock unloading, hydraulic fracturing, gas loss by sublimation and freeze–thaw.

Thermal expansion cracking has been proposed as an explanation for particle ejection from the regolith of Bennu[11] and might generate surface-correlated fractures through differences in solar insolation. Although sample A0180 was collected on the current surface of Ryugu, the presence of an aqueous fluid phase within the observed fractures, however, precludes their formation near the surface of the asteroid where sublimation would occur. As a rubble-pile surface, materials on Ryugu can sample any depth within the progenitor asteroid[10]. Thermal fracturing by internal heating of asteroids furthermore occurs by dehydration during metamorphism rather than during low-temperature aqueous alteration.

Sublimation of ice or water in the subsurface might also cause fracturing, with wet and dry cycles potentially allowing limited aqueous alteration as observed in cracks in A0180. Nakamura et al.[12] have suggested this process could operate in the near surface of the Ryugu progenitor but would result in explosive degassing and fragmentation, which would be unlikely to preserve fragile structures such as the crack networks observed in A0180. Nevertheless, as open fractures, the cracks in sample A0180 must have lost their ice through gradual sublimation, possibly as burial depth decreased owing to erosional gardening of the surface of the asteroid.

Shock unloading causes extension during pressure release. Extensional shock fractures have been observed in quartz[13], with curved morphologies forming as a result of the passage of the pressure release wave through individual crystals. Likewise, extensional fractures with high tortuosity form during shock unloading close to a free surface and are related to spalling[14]. These fractures are subparallel to the surface with a tortuosity having similar length scales to grain size, owing to the mechanical heterogeneity of granular materials[14]. In A0180, however, average grain size is much smaller (<1 µm) than the length scales of crack tortuosity. Furthermore, cross-cutting extensional fractures are not consistent with their formation subparallel to a free surface, making it unlikely they formed as a result of spalling. Finally, micro-faults with shear displacement found in Ryugu have been suggested to form as a result of mild shock[15]; however, these fractures are subplanar and have very low tortuosities (~1.02) and wavelengths (<100 µm) and, thus, have a very different morphology to the fractures and veins described here.

Hydraulic fragmentation within asteroids during aqueous alteration could occur if fluids develop overpressures that exceed the tensile strength of the matrix and overburden. Aqueous alteration seals pores and produces barriers to fluid migration that could result in overpressures in liquids. The ingress of distal fluids at elevated pressure can, however, be discounted since it cannot explain the presence of isolated fractures completely enclosed by crack terminations. Furthermore, hydraulic fragmentation is typically associated with brecciation[16], which is not present in this sample comprising a homogeneous

Fig. 1 | Backscattered electron and nano-XCT slice images showing veins and fractures. a, Subparallel fractures (F) with alteration halos (mR). One fracture (dF) is deflected around a dolomite crystal (Dol) and truncates a lenticular cluster of framboidal magnetite (fM). Spheroidal magnetite (sM) and sulfide crystals (S) are also present. **b**, Several subparallel fractures with alteration halos (mR). A sudden deflection in a fracture tip occurs in two nearby fractures. A perpendicular set of fractures also occurs (pF). **c**, An isolated fracture with a cuspate morphology (CF). One end of the fracture is infilled by phyllosilicates (hF). The fracture is surrounded by a metasomatic halo (mR). **d**, Sulfide infilling a fracture (S) adjacent to a dolomite crystal. The sulfide has an irregular margin against matrix suggesting it grew within the fracture. **e**, An elongate vein (mV) containing framboidal magnetite (fM). A second vein mantles one side of a hydrated silicate grain (mM). A small portion of a fracture (F) appears in-line with the end of the vein. **f**, Three cross-cutting veins. Two veins are decorated with magnetite (mV), while one has a central, partially infilled fracture (hF) with an alteration halo (hF). **g**,**h**, CT slices showing a range of different morphologies, including cuspate cross-cutting magnetite veins (mV) (**g**) and sinuous (SF) magnetite veins (mV) (**h**). Isolated fractures (iF) are also present. **i**–**k**, Matching BEI (**i**) showing metasomatic aureole (mA) around fractures and the margins of the particle and wavelength-dispersive spectroscopy X-ray maps of Mg (**j**) and Na (**k**). The colour scale of the maps shows composition in wt% from the maximum value to zero (a Si map is provided in Supplementary Fig. 4). **l**, A high-resolution X-ray map showing coarse phyllosilicates (cP) overgrowing an open fracture. The fracture contains elevated carbon abundances despite not containing mounting resin. The locations within the sections of the sample are shown in Supplementary Fig. 5.

https://doi.org/10.1038/s41550-024-02369-7

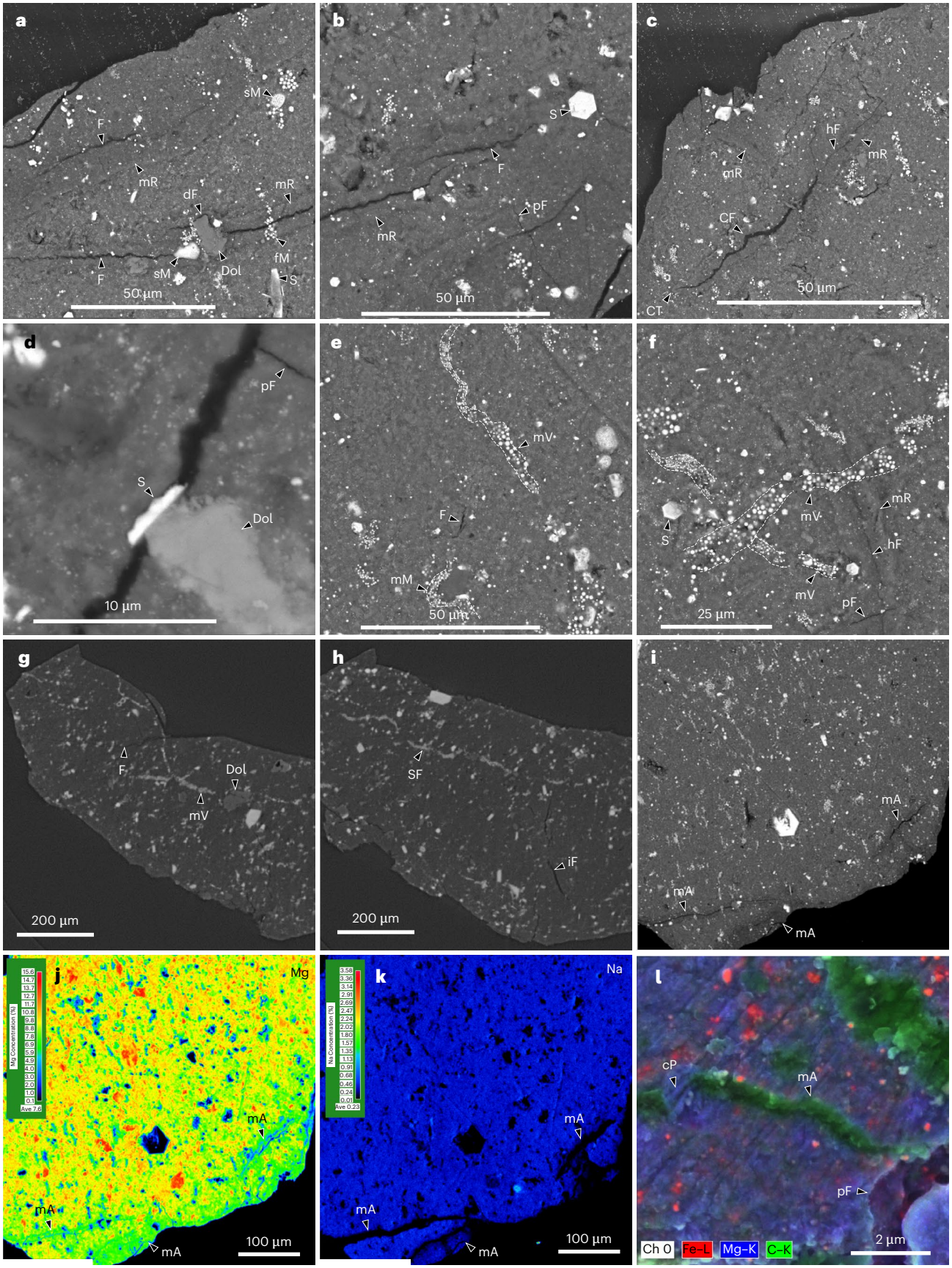

https://doi.org/10.1038/s41550-024-02369-7

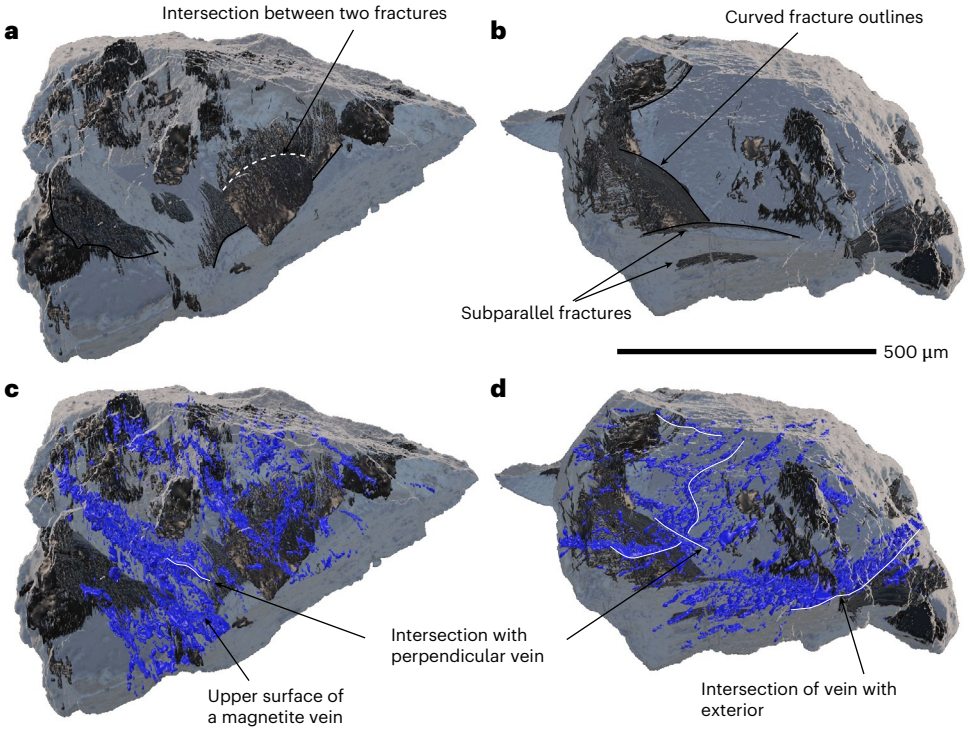

Fig. 2 | 3D reconstructions of fractures and magnetite veins in perspective view created from nano-CT data. Fractures are shown in black and magnetite veins in blue. Both fractures and magnetite veins have curved, intersecting morphologies dominated by cuspate forms. Some magnetite veins are cut by fractures; others are subparallel. Lines have been added to emphasize the 3D shape and intersection of features. **a** and **b** show fractures, while **c** and **d** also include magnetite veins. **a** and **c** are projected from the left, while **b** and **c** are projected from the front.

lithology, although it has been observed in CM2 chondrites[17]. Some other Ryugu samples are polymict breccias, most likely formed by shock fragmentation[12,18]. The presence of networks of submicrometre phyllosilicate veins within the matrix of one sample suggests brecciation at a late stage in aqueous alteration[19].

Freeze–thaw causes fracturing owing to the 9% volume change during the ice-to-water phase transition[20], although in detail the process is complex since it involves the pressure of crystallization of ice, and hydraulic fragmentation by unfrozen water, with overpressures generated by ice growth, capillary effects and water vapour production mediated by the Gibbs–Thompson effect[20]. In terrestrial permafrost and frozen soils, ice lenses and wedges form by migration of fluids owing to the magnitude of gravity-driven overburden and cryogenic suction[21].

In microgravity, freeze–thaw is likely to be dominated by the effects of expansion and contraction, rather than the buoyancy-driven migration of fluids. During freezing, expansion generates compressive radial and extensional concentric stress around ice grains, resulting in the formation of radial fractures (Fig. 3). Transport of water during freeze cycles, however, will be limited to thin fluid films of unfrozen water—liquids that can survive up to −20 °C owing to the chemical potential at mineral surfaces and the presence of solutes[22]. In contrast, thaw cycles cause contraction generating compressive concentric stress, which closes radial fractures, and extensional radial stress, opening concentric fractures. Pore fluids will readily accumulate within these fractures owing to the elevated temperatures and may grow by crack tip propagation if hydraulic pressure is sufficient. Indeed, in microgravity, crack propagation could be expected to be efficient since overburden is minimized, and overpressure merely needs to exceed the tensile strength of the matrix.

Freeze–thaw experiments were performed using ice grains embedded in clay to investigate the nature of fractures. The results showed that cross-cutting radial and concentric fractures indeed form during freeze–thaw, albeit with modification during later freeze–thaw cycles owing to the dispersion of ice within veins. Furthermore, the fractures typically have cuspate or sinusoidal forms with similar tortuosity to those observed in Ryugu (1.30–1.05). The tortuosity forms as a result of variations in principle stress as a result of expansion of ice present in surrounding veins. Other studies of freeze–thaw in soils and sedimentary rocks also show similar tortuosity in fractures[23–25].

The morphology of cracks and magnetite veins in Ryugu agrees well with the expected behaviour of fracturing during freeze–thaw. Subordinate cracks perpendicular to larger fractures are consistent with the formation of radial fractures during freezing, while the dominant curved fractures form during thaw cycles. The freeze–thaw model also explains the formation of subparallel isolated curved fractures (Fig. 3a), with some break-through occurring, and divergence from curved morphologies, owing to stress interference between crack tips[26]. Finally, cavities observed within Ryugu samples have tentatively been suggested to have contained ice[27].

Freeze–thaw has previously been suggested to explain compressive fabrics observed within CI chondrites[28] and Ryugu[12] and has been discussed as a theoretical mechanism that could operate during the aqueous alteration of carbonaceous asteroids[29,30]. Until now, however, no evidence for freeze–thaw fractures has been recognized, even though similar cracks have been observed in Ryugu samples[12] (Fig. 1c). The fractures and veins in A0180 strongly suggest that freeze–thaw occurred in the Ryugu progenitor and furthermore is consistent with the low temperatures predicted for its aqueous alteration of 0–20 °C, which make it susceptible to refreezing during temperature fluctuations[31].

Freeze–thaw cycles within asteroids are a natural consequence of temperature fluctuations resulting from the different timescales of heat transport by fluid migration and conduction. The outwards migration of fluids delivers heat to regions closer to the surface, which melts primordial ice, followed by cooling as a result of heat loss by

https://doi.org/10.1038/s41550-024-02369-7

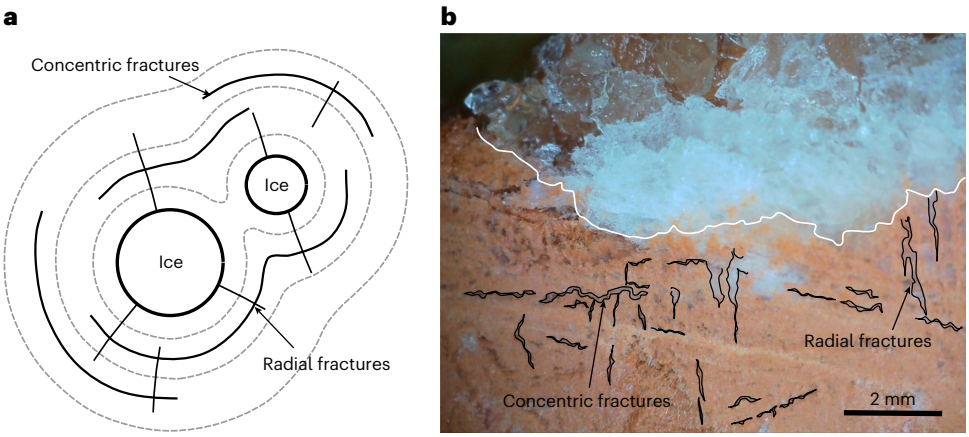

Fig. 3 | The nature of freeze–thaw fractures around ice grains. **a**, A schematic diagram showing the predicted geometries of concentric and radial extensional fractures (black lines) formed by stress interference by expansion and contraction of ice grains. The dashed grey lines show stress contours. **b**, A photograph of the results of freeze–thaw experiments showing radial (perpendicular to ice grain boundary) and concentric (subparallel to ice grain boundary) fractures developed around an ice grain in clay. The margins of the ice grain are denoted by the white line. Concentric fractures are tortuous. This experiment involved three cycles of freeze–thaw. The geometries of fractures are modified by dispersed ice compared with the idealized example.

conduction. The sealing of migration pathways by precipitation of phyllosilicates and carbonates, followed by hydraulic and/or shock fragmentation, will result in pulses of rising fluids that generate transient heating, causing multiple freeze–thaw cycles. The number of freeze–thaw cycles in the region of the Ryugu progenitor sampled by A0180 was limited, with the veins and fractures requiring at least two cycles.

Asteroid-wide transport of fluids could be facilitated by freeze–thaw fractures if these can be generated at depth within the body. Freeze–thaw occurs at the outer fringes of the expanding shell of melt water, at the interface with the ice-bearing outer layers. Consequently, as melting proceeds, owing to internal heating, the migration of water occurs utilizing fractures already generated by freeze–thaw. As long as the overburden is less than the pressure exerted by ice growth, freeze–thaw can cause fracturing. The disjoining pressure within thin liquid films surrounding growing ice is estimated at 10 MPa (ref. 32)—larger than the tensile strength of Ryugu of 3–8 MPa (ref. 33), allowing freeze–thaw fracturing to occur under overburdens of <7–2 MPa. In a Ryugu progenitor with a density of 1.2 g cm^{-3} (ref. 34) and strength of 8 MPa, this overburden corresponds to the full depth of a 350-km-diameter body, while in a body with a density 1.6 g cm^{-3}, similar to the CI chondrite Orgueil[35], a value of 265 km is obtained. Freeze–thaw will, therefore, produce fracture pathways for fluids through the full depth of most primitive asteroids. Thus, freeze–thaw is likely to play a crucial role in the aqueous alteration of all ice-bearing primitive bodies subjected to sufficient interior heating by increasing its mobility, resulting in wider-spread hydration of asteroidal materials. Rare, well-developed veins filled with drusy phyllosilicate in the CI chondrite Orgueil[36] share some similarities with the fractures observed here, since they are likewise tortuous and contain coarse hydrous minerals precipitated from fluid. In Orgueil, however, phyllosilicate veins form interconnected networks and are wider (up to 20 µm), suggesting extension under higher fluid pressures and growth to form interconnected networks at a more advanced stage in aqueous alteration; their tortuous morphologies might, however, indicate they utilized fractures initially formed by freeze–thaw. Sample A0180 preserves an early stage in this process, with its relatively low abundance of sulfide, magnetite and carbonate compared with other Ryugu samples, testifying to less intense alteration.

Freeze–thaw also provides a mechanism for the repeated release and mixing of fluids within a parent body. The observation of early magnetite veins in A0180, for example, indicates the migration of distal fluids from depth, while the metasomatism of matrix surrounding fractures indicates a second influx of fluid, confirming that episodic ingress of liquids occurred to deliver the heat required for freeze–thaw. The oxygen isotope compositions of CI and CM2 chondrites, which are samples of hydrated, carbonaceous asteroids, also testify to the influx of separate fluids. Phyllosilicates and carbonates fall on the same mass fractionation line in these meteorites, indicating they were in equilibrium with the same aqueous fluid; however, magnetite lies on a separate fractionation line indicating a distinct fluid phase[37]. Studies of Ryugu samples show that early magnetite is out of equilibrium with the later phyllosilicates and carbonates, with progressive equilibration occurring with time[31]. Distal fluids rising from depth could be out of equilibrium with water generated by localized melting of ice, owing to different degrees of equilibration between ^{18}O-rich water and ^{16}O-rich solids[31]. Alternatively, distal fluids could sample isotopically distinct reservoirs of ice accreted earlier in the growth of the parent body, at greater heliocentric distances, owing to the inwards migration of bodies caused by drag in nebula gas[38]. Aqueous alteration products might, therefore, preserve an isotopic record of the stratigraphy of ice formed in different parts of the solar nebula.

Methods

Sample preparation

Sample A0180 is from chamber A collected from the surface of the regolith of asteroid Ryugu (https://darts.isas.jaxa.jp/curation/hayabusa2/allDescription.php?sample_id=996). It was obtained from Japan Aerospace Exploration Agency (JAXA) in a sealed container in a nitrogen atmosphere. The initial morphological inspection was conducted for the sample exterior through the container window, with the Captured Particles Locating, Observing, Extraction System (CLOXS) digital optical microscope system on automated digital sample stages developed at JAXA/Institute of Space and Astronautical Science (ISAS)[39] (Supplementary Fig. 1). The sample was decanted for nano-XCT. During the mounting process, the sample split into two along fractures (parts A and B). Sample B was mounted for observation.

After nano-XCT analysis, the sample was embedded in a Specifix resin and polished under ethanediol with 0.1 µm aluminium oxide. The sample was stored in a desiccator before SEM analysis and in a sealed sample contained after analysis. The polished block was carbon-coated before SEM analysis. After 8 weeks, the sample was repolished to remove the carbon coat and the new plane of section was imaged by SEM.

Nano-XCT analyses

The Ryugu subsamples (A/B) were mounted in pipette tips and scanned using a Zeiss Versa X-ray micro-computed tomography scanner. X-rays were generated from a tungsten source, with a voltage of 90 kV and a current of 89 µA, using the inbuilt LE4 filter to reduce beam-hardening effects. For each scan, 2,401 projections were collected across a 360° rotation. Each projection was magnified by a 4× objective lens and recorded using a 2,000 × 2,000 charge-coupled device plane (16-bit pixel depth) at exposure times of 33 s and 28 s for A0180-A and A0180-B, respectively, with no binning. Spatial resolutions (in voxels) were 0.625 µm for A0180-A and 0.672 µm for A0180-B. Image stacks were created using the Zeiss Reconstructor software.

CT segmentation and data processing

Nano-XCT data were segmented using ImageJ and Avizo to generate 3D models of specific textural and mineralogical features. The plugin 3D Suite[40] was used to measure sizes from pre-segmented images. The segmentation techniques used varied depending on the feature analysed owing to X-ray absorption contrast between phases. Initial manual segmentation was performed to mask the exterior of the sample to ensure noise outside the sample was not selected. This step greatly simplified 3D model reconstruction. An initial threshold segmentation was performed on the masked data to determine the volume of the particle, giving a value of 0.077 mm^3.

Cavities are observed in computed tomography (CT) data as regions with low X-ray absorption and complicate the segmentation of fractures. Fractures were manually masked to separate them from cavities. This process means that fractures cut by cavities introduce uncertainties; however, inspection of the two sections cut through the specimen suggests <1% of the length fractures intersect cavities.

To ensure optimal segmentation by thresholding, the area selected was monitored versus red–green–blue (RGB) value and a value was chosen where little change in area occurred with threshold. Nevertheless, thresholding does result in noise selection. The ImageJ Remove Outliers tool was used to remove any selected volume less than 2 voxels in size.

The uncertainty of manual thresholding was investigated by examining the precision of measurements obtained by repeat segmentation of a cavity. The results are shown in Supplementary Fig. 2 and Supplementary Table 1 and suggest uncertainties are <10% of void size. Furthermore, the cumulative size distributions of the voids provide a good fit to exponential trendlines and give confidence that measurement uncertainties are small.

Magnetite and sulfide were both segmented by the RGB threshold, and outliers were removed to reduce the effects on noise. Sulfide has high X-ray absorption and could be reliably segmented by thresholding. Magnetite has lower X-ray absorption with areas consisting of mixtures of framboidal magnetite and matrix. These areas have absorption higher than matrix and dolomite. However, edge effects around sulfides (lower X-ray absorption in voxels that overlap sulfide and surrounding material) are within the range of magnetite. To remove edge effects, the sulfide mask was increased by 1 voxel using ImageJ's grow function and then used to mask out the edges. The uncertainty caused by the removal of edge effects was investigated by increasing sulfide volumes by 2 voxels; the results indicate a less than 0.1% decrease in magnetite volume.

Magnetite in the specimen occurs as both spheroidal magnetite, with radiating internal textures, and clusters of framboidal magnetite. Spheroids were segmented by sphericity using a value of >0.8. The spheroidal magnetite mask was then subtracted to obtain the volume of framboidal magnetite. The resulting framboidal magnetite volume actually represents a mixture of magnetite and matrix. To delimit the volume of magnetite framboids, the abundance of magnetite in these areas was measured in backscattered electron images by thresholding, giving an average of 36.5% of the area of images with a range of 32.9–41.2%. Dolomite can be observed in the CT imagery but has X-ray absorption that overlaps with matrix. The dolomite was not segmented, nor its volume measured.

Magnetite veins are a mixture of framboidal magnetite and matrix and have lower X-ray absorption than magnetite alone. Spheroidal magnetite, which has radiating internal textures and larger size than framboidal magnetite, is also present in some veins. Magnetite veins were segmented by manual masking on the basis of the large aspect ratios (>10); consequently, short segments of magnetite veins may have been excluded from the segmentation. The volume of magnetite veins is, therefore, a minimum estimate. The uncertainty in measurement of the abundance of phases and fractures from nano-XCT data was estimated by varying thresholds and is approximately 1%.

SEM

SEM was performed on a polished block using a Hitachi TM4000Pro Desktop SEM at Imperial College London. Backscattered electron images were collected at an accelerating voltage of 15 kV and have resolutions of up to 7 nm per pixel with some variation due to working distance. Semi-quantitative analyses were obtained by energy-dispersive spectroscopy using an Oxford Instruments AZtec series silicon drift detector with an energy resolution of 151 eV (Cu-Kα). Analyses were performed at an accelerating voltage of 20 kV using a beam current of 2 nA. No gain calibration was applied, and thus, analytical totals are not quantitative. Oxford instruments matrix corrections were used against factory standards. Uncertainty in elemental ratios was evaluated by analyses of San Carlo olivine and are <5% for major elements (Mg, Al, Fe and Si) and <20% for minor elements (Ca, Mn and Ni). Detection limits are ~0.1 wt% on carbon-coated, polished sections.

Electron microprobe element maps were collected with the JEOL JXA-8530F Hyperprobe operating in wavelength-dispersive spectrometry mode at 15 kV voltage and 100 nA current, with a dwell time of 100 ms per pixel, using a 1 µm beam diameter at 1 µm spacing.

Measurement of tortuosity

Tortuosity was measured on backscattered electron images and on XCT slices. The measurement was obtained by determining the length of a straight line connecting two points on the fracture and length of a path running along the centre of fractures. The tortuosity is the ratio of path length to line length. Measurements were made in ImageJ. Uncertainties were determined by repeat measurement and vary between 2% and 5% with higher values for shorter fractures.

Calculation of maximum asteroid size

The maximum size of an asteroid that could undergo freeze–thaw was calculated using a simple model for the pressure P at the core of a spherical uncompressible body of radius r with a constant density ρ (equation (1)).

$$P = \frac{2}{3} G\rho^2 r^2 \quad (1)$$

A radius threshold R for fracturing by ice was evaluated assuming that an overburden less than the disjoining pressure of liquid films on ice (10 Ma) minus the tensile strength of Ryugu (8 MPa) as shown in equation (2).

$$R < \sqrt{\frac{3P}{2G\rho^2}} \quad (2)$$

Freeze–thaw experiments

Experiments were performed to quantify the morphology of fractures formed during freeze–thaw. An experimental cell was constructed consisting of an ice grain of known shape and volume surrounded by a fine-grained phyllosilicate matrix contained within a cubic plastic container. An ice grain was generated by freezing water in a mould.

The ice grains shape comprised a hemispherical apex over a cylinder with a circumference that increased to a flat base. The sides of the cylinder sloped at 10° and had a median circumference of ~1.5 cm. The experimental cell was 8 cm in diameter. A large ice grain was chosen to simplify recovery and sample preparation of the experimental charge. The ice grain was pressed into modelling clay purchased from DAS and immediately placed into a freezer at −30 °C to minimize the melting of ice before the experiment. Some shape changes may have occurred before freeze–thaw while the experimental cell equilibrated.

Experiments were performed by removing the frozen cell and heating it at room temperature (10–12 °C). No attempt was made to control the heating rate during melting. The experimental cell was left for 3 h to melt throughout. One experiment was cut while at room temperature to ensure all the ice in the grain and matrix had melted after 3 h.

The freezing cycle was performed by cooling the cell to 2 °C for 8 h to minimize the cooling rate during freezing. Once equilibrated to 2 °C, the cell was placed in a freezer on a spacer to decrease the temperature gradient through the cell. This method was developed after preliminary experiments revealed the presence of vertically oriented needle ice that caused a vertical heave of the ice and a horizontal contraction. Needle ice forms as a result of a temperature gradient and exerts the majority of its crystallization pressure parallel to the orientation of the needle. In preliminary experiments, the cell was cooled rapidly directly from room temperature on the cold plate in the freezer. Experiments with the cubic cell and spacer resulted in mostly equant ice crystals with acicular ice crystals present in only small areas close to the margins of the ice grain.

After three to four episodes of freeze–thaw, the experimental cell was recovered and was cleaved using a heavy blade while still frozen. The cell was cut vertically first and broke along a subvertical fracture to expose the remnant ice grain, usually the lower half of the ice grain fragmented during cutting. One-half of the cell was then cut horizontally across the median of the grain.

Results of the experiments are shown in Supplementary Fig. 3 for an experimental charge that experienced three episodes of freeze–thaw. Supplementary Fig. 3a shows the horizontal section across the ice grain, while Supplementary Fig. 3b shows the vertical section, with the broken lower surface above the base of the ice grain. Clay containing veins of ice surround the ice crystal and are variably developed. Veins testify to the loss of water from the ice crystal during both melting and freezing episodes. The recovered pieces and observed areas of ice veins suggest a <5% decrease in ice volume over three episodes of freeze–thaw, suggesting ice volume is preserved to a reasonable degree. Ice shape also resembles the initial ice grain; in particular, the horizontal section retains the original circular outline, although minor protrusions are observed. The vertical sections show more modification but retain the overall shape showing a rounded apex and a flat base with a sudden change in orientation marking the junction between the base and the cylindrical walls (Supplementary Fig. 3).

The formation of protrusions of ice that modify the original ice grain indicate a decrease in sphericity in the experiments of up to 20%. The presence of small areas of needle ice in some protrusions may suggest that these arise in part owing to a temperature gradient during ice freezing and may be less prominent with decreasing cooling rate. Given the transport of heat by distal water into areas containing ice on primitive asteroids, the cooling rate is likely to be exceedingly low since the distal water is likely to have been cooled by matrix ice during migration and will initially be at 0 °C.

Fractures filled with ice are formed by expansion and contraction during freeze–thaw. Expansion during freezing exerts a crystallization pressure of ~10 MPa resulting in compression perpendicular to the margins of the ice grain (radial compression) and extension parallel to surfaces (concentric extension). Radial veins of ice approximately perpendicular to the clay–ice boundary can be seen in Supplementary Fig. 3c,d. During melting, the grain contracts, resulting an extension perpendicular to the water–clay boundary (radial extension) and compression parallel to the surface (concentric compression). This results in extensional concentric fractures. In the experimental charges, concentric veins are subparallel to the margins of the ice grain; however, expansion of ice within veins formed in earlier freeze–thaw cycles modifies their orientations.

The availability of water during melting would be expected to result in better development of concentric extensional fractures than radial fractures that form during melting. In the experimental charge, radial veins are thinner in those areas with well-developed concentric veins. Some well-developed radial veins are, however, present. The presence of temperature gradients during the experiments, related to the relatively large cooling rates, may result in higher amounts of water being available during freezing than would occur under slow cooling. The availability of water may enhance the development of radial veins in the experiments. The morphology of the veins is quite variable; however, most are tortuous and show wavelengths of ~0.5 mm.

Data availability

The whole Ryugu Sample Database is available from https://www.darts.isas.jaxa.jp/curation/hayabusa2/. The Hayabusa2 Ryugu sample curatorial dataset is also referenced at https://doi.org/10.17597/ISAS.DARTS/CUR-Ryugu-description. Raw nano-XCT data are available for download via Figshare at https://figshare.com/s/eacc0dafe459529093c1 (4 GB). An interactive 3D reconstruction of the nano-XCT data is also available for Windows 64-bit (https://figshare.com/s/e38983711f244402bc9b; 49 MB) and Mac 64-bit (https://figshare.com/s/21863cc207c42e448462; 58 MB). All other data are provided in Supplementary Information.

References

1. Ciesla, F. J. & Cuzzi, J. N. The evolution of the water distribution in a viscous protoplanetary disk. *Icarus* **181**, 178–204 (2020).
2. Weidenschilling, S. J. Accretion of the asteroids: implications for their thermal evolution. *Meteorit. Planet. Sci.* **54**, 1115–1132 (2019).
3. Brearley, A. J. in *Meteorites and the Early Solar System II* (eds Lauretta, D. S. & McSween, H. Y.) 587–624 (University of Arizona Press, 2006).
4. Alexander, C. M. et al. Elemental, isotopic and structural changes in Tagish Lake insoluble organic matter produced by parent body processes. *Meteorit. Planet. Sci.* **49**, 503–525 (2014).
5. Chyba, C. & Sagan, C. Endogenous production, exogenous delivery and impact-shock synthesis of organic molecules: an inventory for the origins of life. *Nature* **355**, 125–132 (1992).
6. Hirabayashi, M. & Tsuda, Y. in *Hayabusa2 Asteroid Sample Return Mission: Technological Innovations and Advances* 572 (Elsevier, 2022).
7. Sawada, H. et al. Hayabusa2 sampler: collection of asteroidal surface material. *Space Sci. Rev.* **208**, 81–106 (2017).
8. Tachibana, S. et al. Pebbles and sand on asteroid (162173) Ryugu: in situ observation and particles returned to Earth. *Science* **375**, 1011–1016 (2022).
9. Watanabe, S. et al. Hayabusa2 arrives at the carbonaceous asteroid 162173 Ryugu—a spinning top-shaped rubble pile. *Science* **364**, 268–272 (2019).
10. Ito, M. et al. A pristine record of outer Solar System materials from asteroid Ryugu's returned sample. *Nat. Astron.* **6**, 1163–1171 (2022).
11. Molaro, J. L. et al. In situ evidence of thermally induced rock breakdown widespread on Bennu's surface. *Nat. Commun.* **11**, 2913 (2020).
12. Nakamura, E. et al. On the origin and evolution of the asteroid Ryugu: a comprehensive geochemical perspective. *Proc. Jpn Acad. B* **98**, 227–282 (2023).

13. Reimold, W. U. et al. Shock deformation confirms the impact origin of the Cerro do Jarau, Rio Grande do Sul, Brazil, structure. *Meteorit. Planet. Sci.* **54**, 2384–2397 (2019).
14. Escobedo, J. P. et al. The effect of shock-wave profile on dynamic brittle failure. *J. Appl. Phys.* **113**, 103506 (2013).
15. Tomioka, N. et al. A history of mild shocks experienced by the regolith particles on hydrated asteroid Ryugu. *Nat. Astron.* **7**, 669–677 (2023).
16. Sachau, T., Bons, P. D. & Gomez-Rivas, E. Transport efficiency and dynamics of hydraulic fracture networks. *Front. Phys.* https://doi.org/10.3389/fphy.2015.00063 (2015).
17. Suttle, M. et al. The Winchcombe meteorite—a regolith breccia from a rubble pile CM chondrite asteroid. *Meteorit. Planet. Sci.* **59**, 1043–1067 (2022).
18. Nakamura, T. et al. Formation and evolution of carbonaceous asteroid Ryugu: direct evidence from returned samples. *Science* **379**, 8671 (2022).
19. Yamaguchi, A. et al. Insight into multi-step geological evolution of C-type asteroids from Ryugu particles. *Nat. Astron.* **7**, 398–405 (2023).
20. Deprez, M., De Kock, T., Schutter, G. D. & Cnudde, V. A review on freeze–thaw action and weathering of rocks. *Earth Sci. Rev.* **203**, 103143 (2020).
21. Fu, Z. et al. Water migration and segregated ice formation in frozen ground: current advances and future perspectives. *Front. Earth Sci*. https://doi.org/10.3389/feart.2022.826961 (2022)
22. Watanabe, K. & Mizoguchi, M. Amount of unfrozen water in frozen porous media saturated with solution. *Cold Reg. Sci. Technol.* **34**, 103–110 (2022).
23. Yang, Z. et al. Experimental study of the freeze thaw characteristics of expansive soil slope models with different initial moisture contents. *Sci. Rep.* **11**, 23177 (2021).
24. Maji, V. & Murton, J. B. Micro-computed tomography imaging and probabilistic modelling of rock fracture by freeze–thaw. *Earth Surf. Process. Landf.* **45**, 666–680 (2020).
25. Leuther, F. & Schluter, S. Impact of freeze–thaw cycles on soil structure and soil hydraulic properties. *Soil* **7**, 179–191 (2021).
26. Wang, H., Tang, L., Yu, S. & Meng, Q. Propagation and interaction of two parallel internal cracks under tensile stress in cuboid glass. *Lithosphere* **4**, 6185359 (2021).
27. Potiszil, C. et al. Insights into the formation of extraterrestrial amino acids from the asteroid Ryugu. *Nat. Commun.* https://doi.org/10.1038/s41467-023-37107-6 (2023).
28. Gounelle, M. & Zolensky, M. E. The Orgueil meteorite: 150 years of history. *Meteorit. Planet. Sci.* **49**, 1769–1794 (2014).
29. Zolensky, M. E. Cyclical regolith processes on hydrous asteroids. *Meteoritics* **30**, 606–607 (1995).
30. Zolensky, M. E. Regolith processes revealed by carbonaceous chondrites with implications for asteroids Ryugu and Bennu, and the martian moon Phobos. In *44th COSPAR Scientific Assembly* Abstract B1.1-0033-22 (2020).
31. McCain, K. A. et al. Early fluid activity on Ryugu inferred by isotopic analyses of carbonates and magnetite. *Nat. Astron.* **7**, 309–317 (2023).
32. Zhuo, T., Mirzadeh, M., Pellenq, R. J.-M. & Bazant, M. Freezing point depression and freeze–thaw damage by nanofluidic salt trapping. *Phys. Rev. Fluids* **5**, 124201 (2020).
33. Kurosawa, K. et al. Tensile (flexural) strength of Ryugu grain C0002. In *53rd Lunar and Planetary Science Conference* abstract number 1378 (2022).
34. Yada, T. et al. Preliminary analysis of the Hayabusa2 samples returned from C-type asteroid Ryugu. *Nat. Astron.* **6**, 214–220 (2022).
35. Consolmagno, G. J. & Britt, D. T. The density and porosity of meteorites from the Vatican collection. *Meteorit. Planet. Sci.* **33**, 1231–1241 (1998).
36. Tomeoka, K. Phyllosilicate veins in a CI meteorite: evidence for aqueous alteration on the parent body. *Nature* **345**, 138–140 (1990).
37. Rowe, M. W., Clayton, R. N. & Mayeda, T. K. Oxygen isotopes in separated components of CI and CM meteorites. *Geochim. Cosmochim. Acta* **58**, 5341–5347 (1994).
38. Kary, D. M., Lissauer, J. J. & Greenzweig, Y. Nebular gas drag and planetary accretion. *Icarus* **106**, 288–307 (1993).
39. Sasaki, S., Imani, J. & Yano, H. Design, fabrication and evaluation of an aerogel processor CLOXS for the astrobiology mission Tanpopo. *Bio. Sci. Space* **33**, 7–11 (2019).
40. Ollion, J., Cochennec, J., Loll, F., Escudé, C. & Boudier, T. TANGO: a generic tool for high-throughput 3D image analysis for studying nuclear organization. *Bioinformatics* **29**, 1840–1841 (2013).

Acknowledgements

The A0180 sample has been loaned to the proposal principal investigator (H.Y.) of this research consortium since 2022, by the JAXA/ISAS Astromaterial Science Research Group through the first international Ryugu sample AO. We thank L. Folco (Univ. Pisa) for useful comments on the manuscript. We are the most grateful for the Hayabusa2 project team to have successfully returned the indigenous samples from Ryugu to the Earth in 2020.

Author contributions

The research was conducted on a sample loaned from JAXA Astromaterial Science Research Group (ASRG) on a proposal for the 1st Announcement of Opportunity for Hayabusa2 samples (AO1), which was led by H.Y., with the other authors as co-investigators. Initial inspection and sample handling were conducted by H.Y. and L.P. Nano-CT data were collected by N.V.A. and processed by M.J.G., M.v.G. and N.V.A. SEM data were acquired by M.J.G. and M.v.G. Freeze–thaw experiments were conducted by M.J.G., M.v.G. and P.J.W. All authors contributed to data interpretation and science discussion. The manuscript was prepared mainly by M.J.G. with contributions from all authors.

Competing interests

The authors declare no competing interests.

Additional information

Supplementary information The online version contains supplementary material available at https://doi.org/10.1038/s41550-024-02369-7.

Correspondence and requests for materials should be addressed to Matthew J. Genge.

Peer review information *Nature Astronomy* thanks Michael Zolensky and the other, anonymous, reviewer(s) for their contribution to the peer review of this work.